

# Interfacial Thermal Conductance between Mechanically Exfoliated Black Phosphorus and SiO<sub>x</sub>: Effect of Thickness and Temperature

Tianyu Wang, Ridong Wang, Pengyu Yuan, Shen Xu, Jing Liu, and Xinwei Wang\*

Black phosphorus (BP) is one of new 2D materials that have attracted wide attention. This work reports the interfacial thermal conductance between BP flake and SiO<sub>x</sub> using Raman spectroscopy. From 293 K down to the 223 K, eight BP flakes in a thickness range of 16.6–113.7 nm are characterized. At 293 K, the largest interfacial thermal conductance is  $1.14 \times 10^8 \text{ W m}^{-2} \text{ K}^{-1}$  for a 82.1 nm thick BP flake, and the smallest one is  $2.17 \times 10^7 \text{ W m}^{-2} \text{ K}^{-1}$  for a 26.6 nm thick BP flake. Such large interfacial thermal conductance can be attributed to the excellent interface contact and strong phonon coupling between BP and SiO<sub>x</sub>. The measured interfacial thermal conductance has a one-fold up to around four-fold increase with decreased temperature from 293 to 223 K, which is a result of thermal-expansion-mismatch induced variation in the morphology of BP flakes. Additionally, it demonstrates no thickness-dependent behavior. It is speculated the intrinsic thickness dependence is weak and is overshadowed by the large variation in the interface contact of different samples. As a new 2D material, BP shows great potential to be a thermal interface material for heat dissipation in electronics.

## 1. Introduction

Black phosphorus (BP), the most stable allotrope of phosphorus, has been rediscovered as a new 2D material due to its remarkable electronic and optical properties. Like graphene and transition metal dichalcogenide (TMDC), few-layered BP can be mechanically exfoliated from its bulk crystals due to the weak van de Waals interaction.<sup>[1]</sup> Few-layered BP field effect transistors (FETs) demonstrate a high on/off ratio and a high carrier mobility.<sup>[2–5]</sup> Furthermore, BP has a tunable thickness-dependent direct band gap from 1.5 eV (monolayer) to 0.3 eV (bulk), which bridges the semimetallic graphene and semiconducting TMDC.<sup>[3,4]</sup> Most intriguingly, BP has an anisotropic

nature in optical, electrical, thermal, and mechanical properties, which has been proved experimentally and theoretically.<sup>[2,4,6–19]</sup> These anisotropic properties are attributed to the unique puckered honeycomb structure of BP single layer, in which each phosphorus atom is covalently bonded to its three adjacent atoms. Commonly, the anisotropic nature of BP is described by its two inplane directions, armchair direction and zigzag direction. The novel properties of BP provide us opportunities for developing new electronic and optoelectronic devices.

Thermal properties, especially the thermal conductivity and interfacial thermal conductance, are of great importance in the design of nanodevices. Owing to the difficulties for fabricating large and thin samples, experimental investigations of thermal properties of BP, especially for few-layered ones, are

still limited.<sup>[11–15]</sup> For the first time, using a micro-Raman spectroscopy, Luo et al. measured the anisotropic thermal conductivity of suspended few-layered BP.<sup>[11]</sup> The thinnest BP flake with a thickness of 9.5 nm has thermal conductivities of  $\approx 10$  and  $\approx 20 \text{ W m}^{-1} \text{ K}^{-1}$  in armchair and zigzag directions respectively.<sup>[11]</sup> Later, Jang et al. reported the measurements of intrinsic thermal conductivities of BP flakes in a thickness of 138–552 nm using conventional time-domain thermoreflectance (TDTR) and beam-offset TDTR.<sup>[12]</sup> Moreover, to understand the anisotropic thermal transport in BP deeply and completely, more work has been done using suspended-pad microdevices,<sup>[13]</sup> frequency-dependent TDTR measurement,<sup>[14]</sup> and four-probe thermal measurement.<sup>[15]</sup> Compared to these investigations on the anisotropic thermal conductivities, the experimental study of interfacial thermal conductance is still rare or even missing. Since most configuration for designing 2D material-based devices utilizes Si substrate, it is worthwhile to study the interfacial thermal conductance between BP flake and Si substrate. Using molecular dynamics simulation, Zhang et al. showed the interfacial thermal conductance between phosphorene (monolayer BP) and Si substrate can be up to  $\approx 6.7 \times 10^7 \text{ W m}^{-2} \text{ K}^{-1}$  at 300 K.<sup>[20]</sup> It suggested phosphorene is an attractive and promising thermal interface material for next-generation nanodevices.

So far, to the best of our knowledge, the experimental study of interfacial thermal conductance between BP flake and

T. Y. Wang, R. D. Wang, P. Y. Yuan, Dr. J. Liu, Prof. X. W. Wang  
 Department of Mechanical Engineering  
 Iowa State University  
 2025 Black Engineering Building, Ames, IA 50010, USA  
 E-mail: xwang3@iastate.edu

Prof. S. Xu  
 Automotive Engineering College  
 Shanghai University of Engineering Science  
 333 Longteng Road, Shanghai 201620, P. R. China

 The ORCID identification number(s) for the author(s) of this article can be found under <https://doi.org/10.1002/admi.201700233>.

DOI: 10.1002/admi.201700233

Si substrate is still missing. Here we report the first experimental investigation using micro-Raman spectroscopy. Strictly speaking, considering the existence of a layer of native oxide on Si surface, the actual interface we study is the BP/SiO<sub>x</sub> interface (SiO<sub>x</sub> represents the thin layer of native oxide on Si surface). By studying BP flakes with thicknesses of 16.6–113.7 nm over a temperature range of 223–293 K, the influence of thickness and temperature on interfacial thermal conductance are explored. The micro-Raman spectroscopy utilizes the variation in Raman spectrum to probe the local temperature rise of laser heating area, and extract interfacial thermal conductance. This technique has been successfully applied to characterize interfacial thermal conductance of graphene/4H-SiC, graphene/Si, graphene/SiO<sub>2</sub>, and MoS<sub>2</sub>/c-Si.<sup>[21–23]</sup> It has been proved to be an effective and reliable method for characterizing interfacial thermal conductance rapidly and nondestructively. Our investigation will advance our understanding of interfacial phonon transport mechanism across the BP/SiO<sub>x</sub> interface, contribute to the development of new nanodevices, as well as benefit future application of BP in electronic industries.

## 2. Experimental Results

Figure 1 shows atomic force microscope (AFM) images of three typical BP flakes we have measured. For each sample, the top figure (e.g., Figure 1a-1) shows the surface morphology, and the bottom one (e.g., Figure 1a-2) shows the height and roughness profile along the white line in the morphology figure. The thickness of these BP flakes is 16.6, 26.4, and 82.1 nm. In contrast to the thick sample, the thin BP flake shows a larger surface roughness, probably caused by the microwrinkles and

oxidation-induced bubbles.<sup>[24–26]</sup> The characterization of surface morphology is of significant importance for explaining the temperature dependence of interfacial thermal conductance. Figure 2a shows the configuration of Raman system applied for performing measurements. Under the illumination of 532 nm laser, Raman peaks corresponding three vibrational modes, A<sub>g</sub><sup>1</sup>, B<sub>2g</sub>, and A<sub>g</sub><sup>2</sup> (Figure 2b) can be observed. Owing to the linear polarization of excitation laser and anisotropic properties of BP, the intensity of Raman peaks will change as the laser polarization angle changes. Figure 2c gives the Raman spectra of 16.6 nm BP flake when the laser polarization is along the armchair and zigzag directions respectively. Three Raman peaks (A<sub>g</sub><sup>1</sup>, B<sub>2g</sub>, and A<sub>g</sub><sup>2</sup>) are located at 360, 437, and 465 cm<sup>-1</sup>, respectively. It can be observed that the intensity of B<sub>2g</sub> and A<sub>g</sub><sup>2</sup> decreases largely under the rotation of laser polarization from the armchair direction to zigzag direction, while the intensity of A<sub>g</sub><sup>1</sup> increases slightly in this process. When the laser polarization is along the armchair direction, the A<sub>g</sub><sup>2</sup> peak has the highest relative intensity. Since the A<sub>g</sub><sup>2</sup> peak is utilized to extract thermal properties, its relative high intensity can suppress the peak fitting errors. Thus, all the Raman measurements are conducted when the laser polarization is along the armchair direction.

The excitation laser power is selected carefully to induce evident temperature rise but avoid any possible damage simultaneously. Since a thickness-dependent temperature rise per unit laser power is observed in the Raman measurements, a large (small) output laser power is employed to irradiate thin (thick) BP flake. For the 16.6 nm BP flake, the thinnest sample we have measured, the output laser power is 75 mW before any attenuation in the optical path. To obtain the variation of Raman peaks against laser power with a low measurement

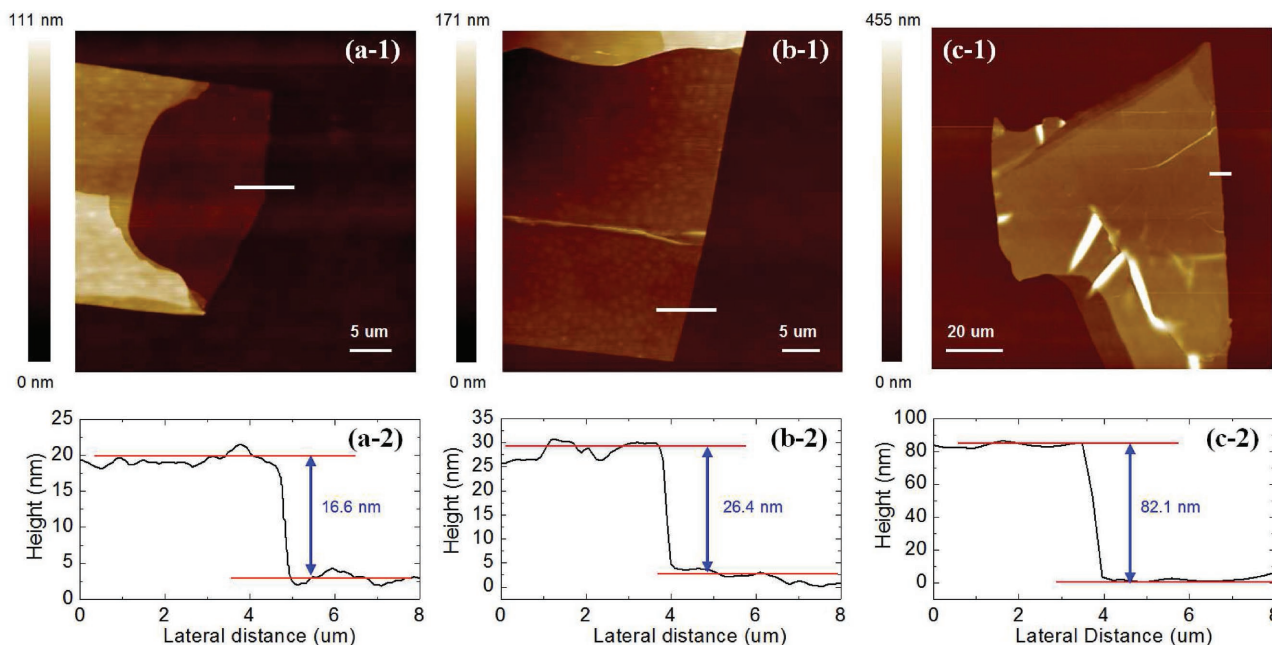


**Figure 1.** The morphology of BP flakes characterized by AFM. The height and roughness profiles are characterized along the white lines in the figures. The thickness is given by the average height of BP surface with respect to the Si substrate. The BP flakes have thicknesses of a) 16.6 nm, b) 26.4 nm, and c) 82.1 nm.

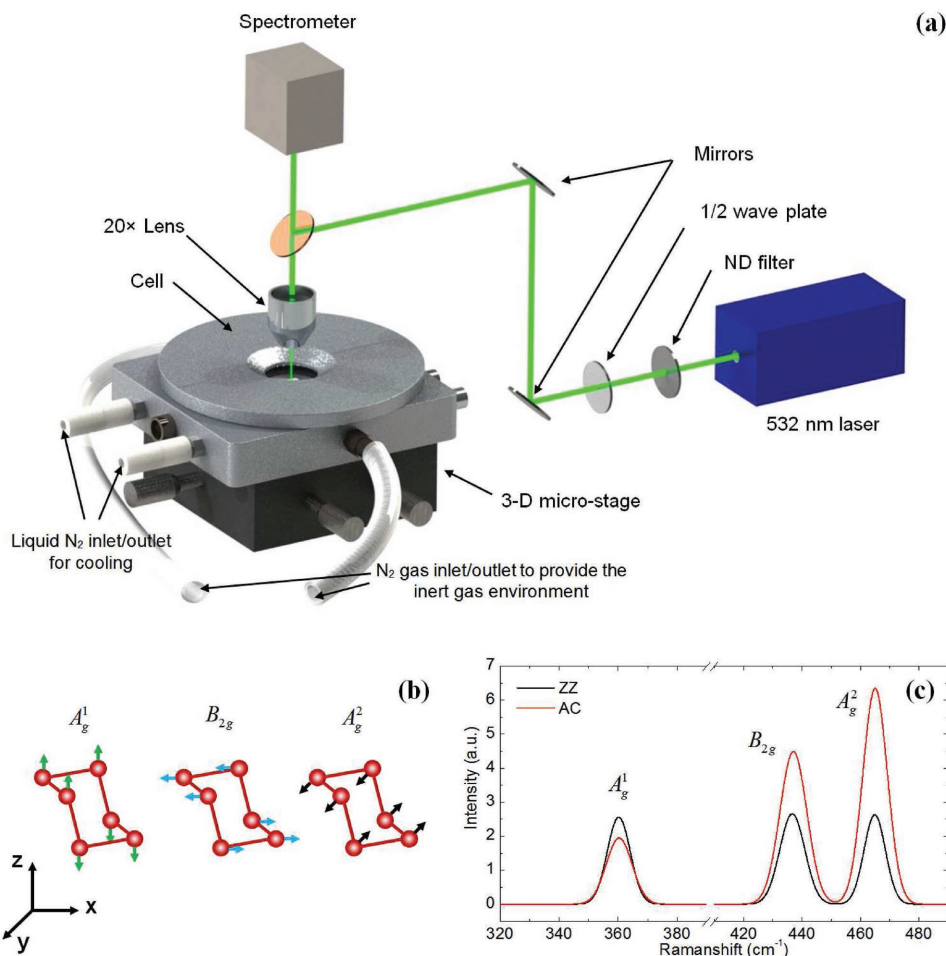


**Figure 2.** a) Schematic of optical system for Raman measurements. The environment cell is mounted on a 3D macrostage. The filling of  $N_2$  gas to the cell chamber is achieved through the gas inlet/outlet. The liquid  $N_2$  inlet/outlet allows the cooling of cell chamber. b) Four phosphorus atoms constitute a unit cell of black phosphorus. Three vibration modes of BP are shown in a unit cell. The armchair direction is along the  $x$  axis, and the zigzag direction is along the  $y$  axis. c) Raman spectra of 16.6 nm BP flake when the laser polarization is along the armchair and zigzag direction, respectively. These Raman spectra have been fitted by the Gaussian function.

uncertainty, a series of laser power from low to high is used to irradiate and heat BP flake. Such adjustment of laser power is achieved through a neutral density (ND) filter with transmission of 0.17, 0.20, 0.25, 0.31, 0.42, 0.53, 0.62, 0.80, and 0.97. Considering the laser energy loss in the optical path and the attenuation of ND filter, the laser power reaching the surface of 16.6 nm BP flake is 9.61, 11.69, 14.57, 18.27, 24.42, 30.81, 36.18, 46.58, and 56.15 mW. Note theoretically we only need to conduct two Raman experiments, one with a lower laser power and one with a higher laser power, to obtain the temperature rise induced by the laser heating. Here we use many different laser powers and linear fitting to significantly suppress the measurement uncertainty. **Figure 3a** shows Raman spectra of the 16.6 nm BP flake excited by above laser powers at 293 K. The accurate positions of Raman peaks are obtained through Gaussian-function fitting as plotted in **Figure 3b**. The variation of Raman peak position against laser power shows strong linearity. All three Raman peaks have a significant red-shift in their positions when the laser power increases. The calculated linear coefficients for the variation of Raman peak positions

against laser power are  $(\partial\omega/\partial P)_{A_g^1} = -0.0186 \pm 0.0032 \text{ cm}^{-1} \text{ mW}^{-1}$ ,  $(\partial\omega/\partial P)_{B_{2g}} = -0.0300 \pm 0.001 \text{ cm}^{-1} \text{ mW}^{-1}$ , and  $(\partial\omega/\partial P)_{A_g^2} = -0.0323 \pm 0.0013 \text{ cm}^{-1} \text{ mW}^{-1}$ , respectively. After we obtain  $\partial\omega/\partial P$ , the actual temperature rise is still unknown. Further calibration is needed to measure the temperature coefficient of Raman shift.

Same Raman measurements are repeated at 223, 233, 243, 253, 263, 273, and 283 K to investigate the temperature dependence of interfacial thermal conductance. From above measurements, Raman spectra excited at the lowest laser power (9.61 mW) can also be used to calculate the temperature coefficient of Raman shift, which is a process known as calibration (**Figure 3c**). Fitted by Gaussian-function, the accurate positions of Raman peaks are extracted and their variation with the temperature change are depicted in **Figure 3d**. The temperature dependence of Raman peak positions can be described by  $\omega = \omega_0 + \chi\theta$ , where  $\omega_0$  is the peak position at room temperature,  $\theta$  is the temperature rise, and  $\chi$  is the temperature coefficient. In the case of 16.6 nm BP flake, its temperature coefficient is  $\chi_{A_g^1} = -0.0179 \pm 0.0018 \text{ cm}^{-1} \text{ K}^{-1}$ ,  $\chi_{B_{2g}} = -0.0260 \pm 0.0013 \text{ cm}^{-1} \text{ K}^{-1}$

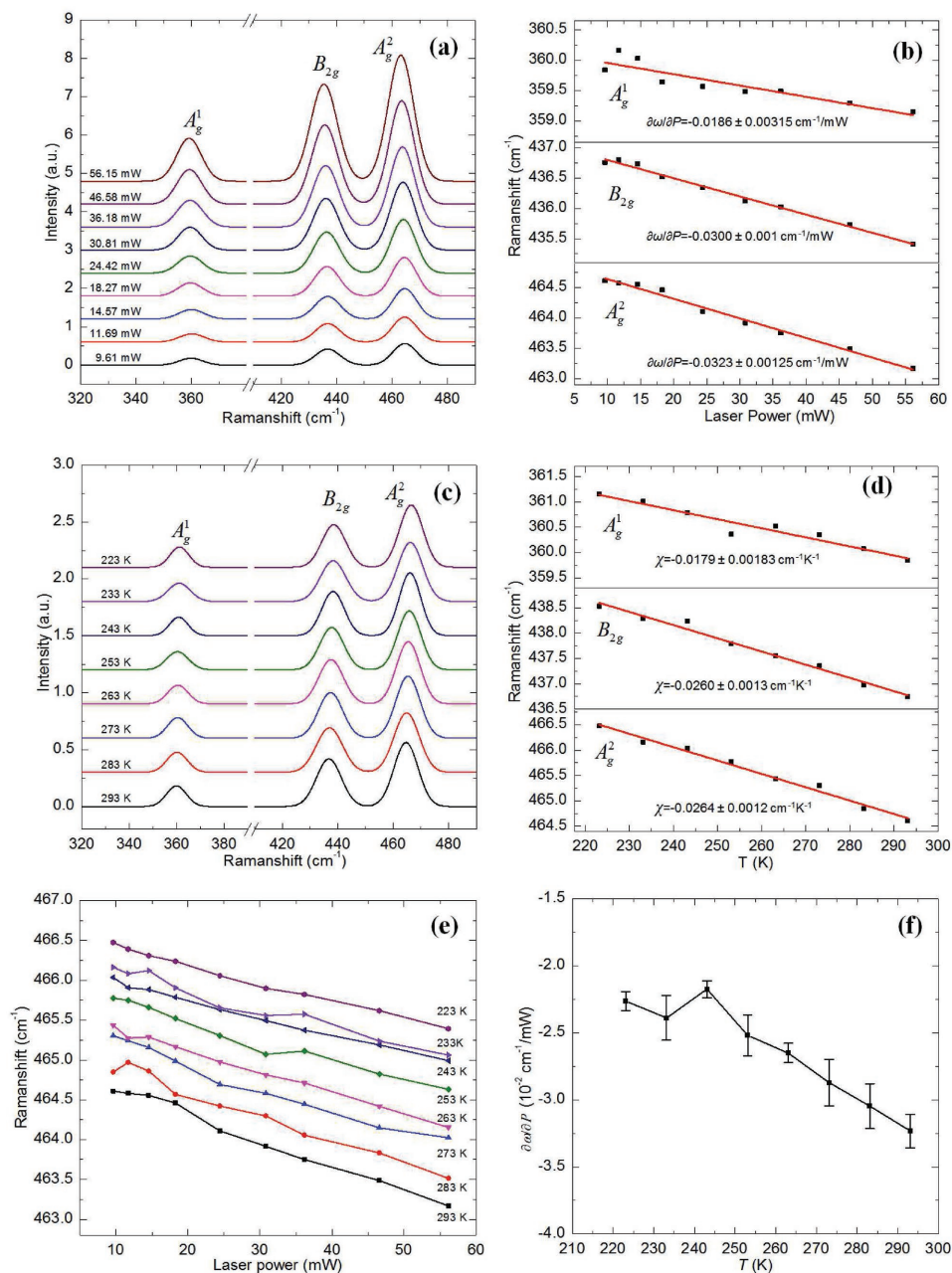


**Figure 3.** a) Gaussian-fitted Raman spectra of 16.6 nm BP flake excited by laser with a power range from 3.64 to 21.27 mW at 293 K. b) The position variation of  $A_g^1$ ,  $B_{2g}$ , and  $A_g^2$  mode Raman peaks of the 16.6 nm BP flake against laser power at 293 K. Their values of  $\partial\omega/\partial P$  are labeled in the figure. c) Gaussian-fitted Raman spectra of 16.6 nm BP flake irradiated by a 9.61 mW laser within a temperature range of 223–293 K. d) The change of  $A_g^1$ ,  $B_{2g}$ , and  $A_g^2$  mode Raman peaks as a function of temperature for the 16.6 nm BP flake when it is irradiated by a 9.61 mW laser. The temperature coefficients of these Raman modes are presented. e) The position variation of  $A_g^2$  mode as a function of excitation laser power at a temperature range from 223 to 293 K. f) The temperature dependence of  $\partial\omega/\partial P$  for the 16.6 nm BP flake. The error bars present the standard deviation of linear fitting.

and  $\chi_{A_g^2} = -0.0264 \pm 0.0012 \text{ cm}^{-1} \text{ K}^{-1}$ . The largest temperature coefficient of  $A_g^2$  among the three Raman modes indicates its strongest temperature sensitivity.<sup>[11,27]</sup> Therefore,  $A_g^2$  mode peak is chosen to do temperature-related Raman analysis and thermal properties calculation. Figure 3e shows the variation of  $A_g^2$  mode Raman peak positions against laser power within a temperature range of 223–293 K. As we expect, the peak position of  $A_g^2$  vibrational mode moves to a low number region at

the increase of excitation laser power, and it moves to large number region at the decrease of temperature. The position variation of  $A_g^2$  mode against laser power at different temperatures is fitted linearly to obtain  $\partial\omega/\partial P$ . Figure 3f clearly displays the decreasing tendency of  $\partial\omega/\partial P$  at the increase of temperature. Based on the value of  $\partial\omega/\partial P$  and  $\chi$ ,  $\partial\theta/\partial P$  can be calculated directly as  $\partial\theta/\partial P = \partial\omega/\partial P \chi^{-1}$ .  $\partial\theta/\partial P$  has the physical meaning of the temperature rise when a laser power of 1 mW

is irradiating on the BP surface. It is the parameter that the interfacial thermal conductance is extracted from. In this study, BP flakes with thickness range of 16.6–113.7 nm are investigated thoroughly, which provides an opportunity for exploring the thickness dependence of interfacial thermal conductance.

### 3. Theoretical Model Development for Heat Conduction

Figure 4a demonstrates the optical absorption model in BP flake. When BP flake is irradiated by an incident laser beam, the transmitted laser beam will experience alternate reflections on the air/BP and BP/Si interface, in which process laser power is absorbed by BP flake. Figure 4b illustrates the thermal transport model of absorbed laser power in the BP flake. The dissipation of laser-induced heat in BP flake is achieved through the inplane and cross-interface thermal transport. Considering the large laser spot size and huge heat sink effect of Si substrate, the thermal transport along the plane of BP flake is small. In our modeling for data processing, the inplane heat conduction is fully considered. The anisotropic inplane thermal conductivity of BP can be simplified to an isotropic one with an equivalent thermal conductivity approximated as an averaged value of armchair and zigzag thermal conductivities. Moreover, the size of BP flakes can be regarded as infinitely large (see Figure S1 in the Supporting Information) due to our large sample size. For the Si substrate, even it has contribution from both laser-induced heating and BP-dissipated heat, its temperature rise is still very small compared to that of BP flake. As we have known, the interfacial thermal conductance is defined as the temperature difference across an interface per unit heat flux. Therefore, the known temperature distribution of BP flake is essential to the extraction of interfacial thermal conductance. In this model, the temperature distribution in a BP flake is obtained from heat diffusion equation in the cylindrical coordinate

$$\kappa_{\parallel} \frac{1}{r} \frac{\partial}{\partial r} \left( r \frac{\partial T}{\partial r} \right) + \kappa_{\perp} \frac{\partial^2 T}{\partial z^2} + \dot{Q} = 0 \quad (1)$$

where  $\kappa_{\parallel}$  is the inplane thermal conductivity of BP flake, and takes a value of  $30 \text{ W m}^{-1} \text{ K}^{-1}$ , estimated from results reported by Luo et al. ( $\kappa_{\text{armchair}} = 20 \text{ W m}^{-1} \text{ K}^{-1}$ , and  $\kappa_{\text{zigzag}} = 40 \text{ W m}^{-1} \text{ K}^{-1}$

for BP flakes with a thickness larger than 15 nm).<sup>[11]</sup>  $\kappa_{\perp}$  is the thermal conductivity of BP flake in the thickness direction, and takes  $4 \text{ W m}^{-1} \text{ K}^{-1}$  in this work.<sup>[12]</sup>  $\dot{Q}$  is the volumetric optical heating with the following expression

$$\dot{Q} = \left[ \frac{I_1}{\tau} e^{-(z/\tau)} + \frac{I_2}{\tau} e^{-(\delta-z)/\tau} \right] e^{(-r^2/r_0^2)} \quad (2)$$

where  $r_0$  is the radius of laser spot,  $\tau$  is the penetration depth in the armchair direction of BP,  $\delta$  is the thickness of the BP flake,  $I_1$  and  $I_2$  are the incident and reflected laser beam intensity (Figure 4a). The  $z$  coordinate and its origin are shown in Figure 4. Note that  $I_1$  and  $I_2$  are calculated considering the multiple reflection of laser and the interference effect using the transfer matrix method (TTM).<sup>[23]</sup> For instance, for this 16.6 nm BP flake, when a 1 mW laser power irradiating the BP surface, 0.578 mW has passed in, and the reflected total energy is 0.0241 mW. Such calculation involves the refractive index and extinction coefficient of few-layered BP in armchair direction which is 3.02 and 1.39 under 532 nm laser illumination.<sup>[7]</sup> The heat conduction in the Si substrate takes the similar treatment as for BP. The thermal conductivity of Si takes  $1.48 \times 10^2 \text{ W m}^{-1} \text{ K}^{-1}$ ,<sup>[28]</sup> and its optical absorption depth takes 882 nm.<sup>[29]</sup> 3D numerical modeling based on the finite difference volume method is conducted to solve the heat conduction in BP and Si, and across BP/Si interface.

The temperature rise obtained from the laser-induced Raman spectra in fact is an average in space weighted by the local Raman intensity. The measured temperature rise of BP can be expressed as

$$\theta_m = \Theta / \Pi \quad (3a)$$

$$\Theta = \int_0^{\delta} \int_0^{\infty} \theta(r) \exp(-r^2/r_0^2) [I_1 \exp(-z/\tau) \gamma_1 + I_2 \exp(-(\delta-z)/\tau) \gamma_2] r dr dz \quad (3b)$$

$$\Pi = \int_0^{\delta} \int_0^{\infty} \exp(-r^2/r_0^2) [I_1 \exp(-z/\tau) \gamma_1 + I_2 \exp(-(\delta-z)/\tau) \gamma_2] r dr dz \quad (3c)$$

Note in the above equations, the coefficients  $\gamma_1$  and  $\gamma_2$  are the attenuation of the Raman signal that is generated at a location

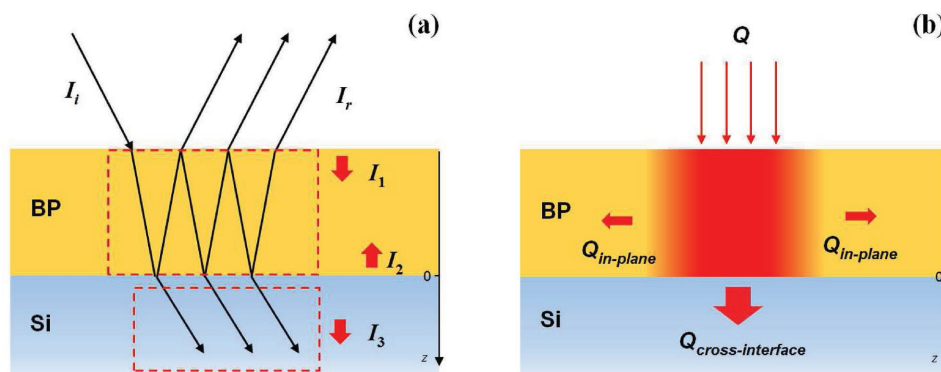


**Figure 4.** a) Optical transmission and reflection model of incident laser beam in multilayer structure. b) Thermal transport model of laser-induced heat in the BP flake. Both inplane and crossplane heat conduction in the BP flake and Si substrate are considered rigorously.

of  $r$  and  $z$ . This attenuation includes the reflection at the BP/Si interface and the secondary absorption in BP flake. All of these have been considered rigorously in the numerical modeling. In our numerical calculation, we apply 1 mW incident laser to calculate the temperature rise of BP flake  $(\partial\theta_m/\partial P)_{\text{theo}}$ . The numerical variation of  $(\partial\theta_m/\partial P)_{\text{theo}}$  as a function of thermal resistance  $R$  (interfacial thermal conductance  $G$  is given by  $G = 1/R$ ) can be obtained by changing the setting value of  $R$  in the model. Finally, measured  $R_m$  can be extracted by linearly interpolating experimental  $\partial\theta/\partial P$  into the numerical variation of  $(\partial\theta_m/\partial P)_{\text{theo}}$  against  $G$  (see Figure S2 in the Supporting Information). In our theoretical model for heat conduction, we assume a pristine silicon without any native oxide. The error introduced by this assumption is analyzed in detail in later sections.

#### 4. Results and Discussion

Figure 5a shows the numerical calculation result of the temperature rise in the 16.6 nm BP flake and Si substrate at 293 K. The temperature rise of the bottom surface of 16.6 nm BP flake and the top surface of Si substrate is depicted in Figure 5a-1. It can be seen the temperature rise of Si surface indeed is very small compared to that of BP flake. What's more, a contour mapping is used to give a clear view of 2D temperature field of BP flake and Si substrate as shown in Figure 5a-2. The calculated Raman weighted temperature rise of Si is  $0.46 \text{ K mW}^{-1}$ , agreeing well with the experimental measured one which is  $0.58 \text{ K mW}^{-1}$ . The contour mapping suggests the existence of large temperature difference across the BP/Si interface. This phenomenon confirms the idea that the interfacial thermal conductance plays a key role for dissipating laser-induced heat. The calculated interfacial thermal conductance ( $G$ ) of all the BP flakes at different temperatures are plotted in Figure 5b. At 293 K, the largest thermal conductance  $G_{\text{max}}$  is  $1.14 \times 10^8 \text{ W m}^{-2} \text{ K}^{-1}$  for the 82.1 nm thick BP flake, and the lowest thermal conductance  $G_{\text{min}}$  is  $2.17 \times 10^7 \text{ W m}^{-2} \text{ K}^{-1}$  for the 26.6 nm thick BP flake. MD simulation of  $\text{SiO}_x$  and its interface with BP has not been reported yet and such work

will require careful construction of the  $\text{SiO}_x$  layer and  $\text{SiO}_x$ -BP interaction. Here we use the reported BP-Si interaction as an instance to demonstrate the local energy coupling. Our results are close to the MD simulation, which showed that the interfacial thermal conductance between phosphorene (monolayer BP) and Si is  $\approx 6.7 \times 10^7 \text{ W m}^{-2} \text{ K}^{-1}$  at 300 K.<sup>[20]</sup> Additionally, MD simulations suggested that the BP and Si systems have strong phonon coupling due to the large overlap of phonon density of state (PDOS). In BP system, phonons in the arm-chair, zigzag and out-of-plane directions are the main energy carriers for thermal transport. Their PDOS has a frequency range of 0–15 THz in which they also have the same peak frequencies. It has been proved that the PDOS of BP system has large overlap with that of silicon system which has a frequency range of 0–18 THz.<sup>[30]</sup> The large PDOS overlap indicates that more phonons are involved in the interfacial thermal transport, and results in a large interfacial thermal conductance. MD simulations deepen our understanding about the high interfacial thermal conductance we have measured, despite BP flake interacts with  $\text{SiO}_x$  rather than Si in our experiment.

As we can see in Figure 5b, all BP flakes show an increasing interfacial thermal conductance with a decreased temperature. For example, the interfacial thermal conductance of 16.6 nm BP flake increases from  $3.62 \times 10^7$  to  $8.27 \times 10^7 \text{ W m}^{-2} \text{ K}^{-1}$  when temperature decreases from 293 to 223 K. It has 129% increase compared to its initial value at 293 K. The largest variation happens on the 82.1 nm BP flake which has 376% increase, and the smallest one happens on the 26.4 nm BP flake which has 77% increase. Detailed information can be found in Table 1. The measured thermal conductance at BP/ $\text{SiO}_x$  interface shows an anomalous temperature-dependent behavior which is contradictory to previous MD simulations.<sup>[20]</sup> By assuming a perfect contact condition, Zhang et al. showed that the interfacial thermal conductance between phosphorene and silicon increases from  $4.4 \times 10^7$  to  $8.7 \times 10^7 \text{ W m}^{-2} \text{ K}^{-1}$  when temperature increases from 150 to 400 K, due to the temperature-dependent behavior of PDOS overlap. However, according to literature review, we noted that Taube et al. reported an exactly same temperature-dependent behavior of interfacial thermal conductance as our

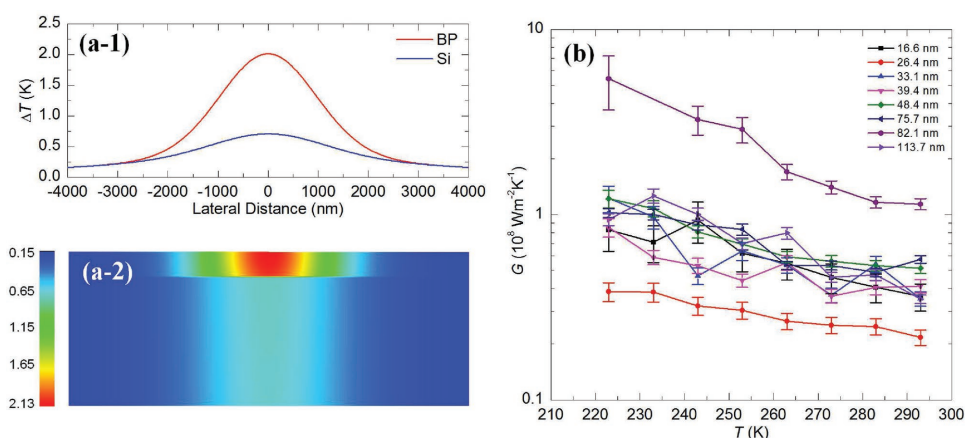


**Figure 5.** a-1) Temperature field of the bottom surface of 16.6 nm BP flake and top surface of Si substrate along the horizontal plane at 293 K. a-2) Contour mapping of temperature field across the interface of a 16.6 nm BP flake and Si substrate at 293 K. b) The variation of interfacial thermal conductance of BP flakes with different thickness against temperature. The error bars represent the measurement uncertainty in this work.

**Table 1.** Interfacial thermal conductance ( $G$ ) of BP flakes at 223 and 293 K. Its increase from 293 to 223 K is also calculated.

| Thickness [nm] | $G_1$ [ $10^7$ W m $^{-2}$ K $^{-1}$ ] 293 K | $G_2$ [ $10^7$ W m $^{-2}$ K $^{-1}$ ] 223 K | Variation percentage of $G_2$ over $G_1$ [%] |
|----------------|--|--|--|
| 16.6           | 3.62   | 8.27   | 128.5  |
| 26.4           | 2.17   | 3.84   | 76.9   |
| 33.1           | 3.52   | 12.26  | 248.3  |
| 39.4           | 4.11   | 8.54   | 107.8  |
| 48.4           | 5.14   | 12.19  | 137.2  |
| 75.7           | 5.73   | 10.23  | 78.8   |
| 82.1           | 11.41  | 54.29  | 375.8  |
| 113.7          | 3.50   | 9.42   | 169.1  |

observation.<sup>[31]</sup> They showed that the interfacial thermal conductance between MoS<sub>2</sub> single layer and SiO<sub>2</sub>/Si substrate has an increasing tendency with a decreased temperature. The coincidence of our results with these of Taube et al. makes us to consider other factors that may lead to the anomalous temperature-dependence of interfacial thermal conductance. Since the existence of micro/nanoscale wrinkles and ripples on BP flakes can result in the presence of voids or separation between BP flakes and Si substrate, the perfect contact condition cannot be applied to describe the real one. Therefore, our observed temperature-dependence of interfacial thermal conductance is a result of morphological variation of supported BP at different temperature which can be further traced back to the thermal expansion mismatch between two adjacent materials.<sup>[32–34]</sup> The thermal expansion coefficient of BP in the armchair direction is  $6.82 \times 10^{-6}$  K $^{-1}$  at 223 K and  $7.09 \times 10^{-6}$  K $^{-1}$  at 293 K, while the one in the zigzag direction is  $1.94 \times 10^{-6}$  K $^{-1}$  at 223 K and  $2.76 \times 10^{-6}$  K $^{-1}$  at 293 K.<sup>[17]</sup> They are always larger than the thermal expansion coefficient of Si which is  $1.76 \times 10^{-6}$  K $^{-1}$  at 223 K and  $2.55 \times 10^{-6}$  K $^{-1}$  at 293 K.<sup>[35]</sup> With the temperature decreases, free-standing BP flakes will have larger contraction than Si. For BP flakes on Si, the strong van der Waals interaction restrains the contraction of BP flake and leads to an inplane tensile strain at low temperatures. The accumulated tensile strain in BP along the armchair and zigzag directions are 0.034% and 0.0014%, respectively when temperature decreases from 293 to 223 K. Under the tensile strain, these wrinkles on the BP flake will be flattened and a more uniform interface contact with reduced separation distance can be achieved. Our previous studies have strongly demonstrated that the interfacial thermal conductance increases rapidly (3 orders of magnitude) with a tiny separation reduction (from 0.7 to 0.4 nm).<sup>[22]</sup> In addition, Huang et al. suggested that an improved topological conformity can significantly enhance the interfacial thermal conductance.<sup>[36]</sup> Hence, we conclude that our observed temperature-dependent behavior of interfacial thermal conductance is largely a result of morphological variation.

In this work, we also try to unveil the relationship between sample thickness and interfacial thermal conductance. The interfacial thermal conductance is intimately related to the characteristics of the interface properties, such as contact condition, atomic bonding and phonon coupling.<sup>[37,38]</sup> Thus, any factors that can influence the interface properties directly or

indirectly will result in the variation of interfacial thermal conductance. Our previous studies have found that MoS<sub>2</sub> has thickness-dependent interfacial thermal conductance.<sup>[23]</sup> Generally speaking, thick MoS<sub>2</sub> has a higher interfacial thermal conductance because the increased mechanical stiffness of thick sample and the resulting improved interface contact. For the interfacial thermal conductance between BP and SiO<sub>x</sub>, we expect the existence of a similar relationship. As shown in Figure 5b, the interfacial thermal conductance of 82.1 and 26.4 nm BP deviates from that of the other samples dramatically. The 82.1 nm BP has the largest interfacial thermal conductance, while the 26.4 nm BP has the smallest one. Additionally, despite the thickness difference between 82.1 and 75.7 nm BP is small, they demonstrate a large variation in thermal conductance. The interfacial thermal conductance of 82.1 nm BP is several times larger than that of 75.6 nm BP. Currently, no clear relationship between BP thickness and interfacial thermal conductance can be identified from our results. This phenomenon may be associated with sample preparation method, which introduces a large morphological variation at BP/SiO<sub>x</sub> interface. Consequently, the intrinsic relationship between interfacial thermal conductance and BP thickness is overshadowed by sample-related variation of interface contact.

#### 4.1. Measurement Uncertainty

One of crucial factors that may influence the accuracy of  $G$  measurement is the nature oxidation of BP in air. In the experiments, despite our samples are made freshly from bulk phosphorus and transferred immediately into an environment cell filled with dry nitrogen gas, they will still be oxidized slightly when candidate BP flake is transferred from viscoelastic stamp to Si substrate. The oxidation effect on the refractive index and extinction coefficient is neglected due to the extremely short air-exposure time (less than 2 min in most cases). However, when BP flakes are characterized by AFM in air after Raman measurements, their oxidation becomes inevitable. Studies have shown that oxidation bubbles form randomly on BP surface by absorbing moisture and oxygen (white bubbles in Figure 1b-1), which have a height larger than its surrounding areas. These bubbles can be recognized easily from AFM height profile. Therefore, the measurement error in thickness can be minimized by interpreting AFM height profile seriously. Although the thickness is determined with great carefulness, its measurement error is still not avoidable due to surface roughness. Here, we calculate the uncertainty of interfacial thermal conductance when the measurement uncertainty of thickness is 2 nm. Besides,  $\partial\omega/\partial P$  and  $\chi$  are other two important parameters for introducing measurement uncertainty. From the standard deviation of  $\partial\omega/\partial P$  and  $\chi$ , their corresponding uncertainty in interfacial thermal conductance can be calculated. Such uncertainty includes the effects like the laser spot drift along BP surface and the out of focus effect of laser spot. By combining the uncertainty introduced by thickness,  $\partial\omega/\partial P$ , and  $\chi$  together, the total uncertainty in interfacial thermal conductance can be obtained, as represented by the error bars in Figure 5b. As we can see in Figure 5b,  $G$  measured from different BP flakes shows a wide dispersion, which

is much larger than the measurement uncertainty. Considering our mechanical method for preparing samples, this phenomenon can only be attributed the large variation in the physical contact of different BP flakes on Si substrate.

The influence of SiO<sub>x</sub> on Si surface on *G* is considered rigorously in this work. When a pure Si is exposed to air, a layer of oxide builds up on its surface rapidly. The stoichiometry and morphology of SiO<sub>x</sub> are not fully understood yet. Most studies suggested that SiO<sub>x</sub> is amorphous and its thickness is ≈2 nm.<sup>[39,40]</sup> When there is a layer of oxide on Si surface, the thermal resistance between BP and Si ( $R_{BP/Si}$ ) is given by  $R_{BP/Si} = R_1 + R_2$ , where  $R_1$  is the thermal resistance between BP and SiO<sub>x</sub>, and  $R_2$  is the thermal resistance of SiO<sub>x</sub>. Also,  $R_2$  is equal to  $l/k$ , in which  $l$  is thickness of SiO<sub>x</sub> and  $k$  is the thermal conductivity of SiO<sub>x</sub>. As a transition between crystalline silicon and amorphous silicon dioxide, the thermal conductivity of SiO<sub>x</sub> is unknown. Here, we assume that the thermal conductivity of SiO<sub>x</sub> is same as that of amorphous silicon dioxide.<sup>[28]</sup> This assumption provides us the lower limit of thermal conductivity of SiO<sub>x</sub>.  $R_2$  is estimated as  $1.45 \times 10^{-9} \text{ m}^2 \text{ K W}^{-1}$  when  $l = 2 \text{ nm}$  and  $k = 1.38 \text{ W m}^{-1} \text{ K}^{-1}$ . Note,  $R_2 = 1.45 \times 10^{-9} \text{ m}^2 \text{ K W}^{-1}$  is the upper limit value. If  $R_2$  is much smaller than  $R_{BP/Si}$  and  $R_1$ , it becomes negligible. Our measured thermal resistances are much larger than  $R_2$  except the 82.1 nm thick BP (see Table S1 in the Supporting information). In other words,  $R_2$  becomes negligible except the 82.1 nm thick BP case. As we can see in Figure 5b, the *G* of 82.1 nm thick BP deviates from that of other samples significantly. The reason of such large deviation is still unclear, but we speculate it may be caused by structure-induced variation in the crossplane thermal conductivity. In our modeling, all the samples use the same crossplane thermal conductivity. If the 82.1 nm BP sample has better structure and a higher crossplane thermal conductivity than other samples, the data processing using a lower crossplane thermal conductivity will lead to a higher interface thermal conductance.

## 5. Conclusion

We investigated the interfacial thermal conductance between BP flakes (16.6–113.7 nm) and SiO<sub>x</sub> at environment temperatures from 223 to 293 K. The whole measurement was conducted in a N<sub>2</sub> atmosphere to prevent oxidation. Our study uncovered a very high interfacial thermal conductance at the BP/SiO<sub>x</sub> interface. At 293 K, the lowest measured *G* is  $2.17 \times 10^7 \text{ W m}^{-2} \text{ K}^{-1}$  for the 26.6 nm BP flake, and the highest one is  $1.14 \times 10^8 \text{ W m}^{-2} \text{ K}^{-1}$  for the 82.1 nm BP flake. Our measurement results agree well with that of molecular dynamics modeling, which showed that the interfacial thermal conductance at phosphorene/Si interface is  $\approx 6.7 \times 10^7 \text{ W m}^{-2} \text{ K}^{-1}$  at 300 K. All the samples show an increasing interfacial thermal conductance when the temperature decreases. Such increase varies from around one-fold up to four-fold. This is attributed to the morphological variation in mechanically exfoliated BP flake due to the thermal expansion mismatch of two adjacent materials. In our study, the interfacial thermal conductance shows little dependence on the BP thickness. It is speculated the intrinsic dependence is weak and is overshadowed by the large variation in the interface contact of different samples. Our results provide the first experimental

clue of the thermal conductance across the BP/SiO<sub>x</sub> interface, which will advance the understanding of phonon transport of this new 2D material and facilitate its application in the design of new electronics.

## 6. Experimental Section

BP flakes were exfoliated from commercially available bulk BP (99.998%, Smart Elements) using a modified mechanical exfoliation method.<sup>[1,41]</sup> The employment of viscoelastic stamp (PF-20/1.5-X4 Gelfilm from Gelpak) in this modified technique reduced the contamination of fabricated BP flakes. Once BP flakes were deposited on stamp, the surface of stamp was examined under an optical microscope to locate a thin BP flake with a large lateral size and uniform color contrast as a candidate for Raman measurements. Supported on the transparent Gelfilm, the thickness of BP flake could be estimated from its color-contrast under normal illumination, which helped to identify the candidate BP flake visually before the determination of accurate thickness by AFM. Then, the candidate BP flake was transferred to a clean Si substrate (rinsed in deionized water and dried in nitrogen gas flow) using a micromanipulator under microscope. A cryogenic environment cell was used to house the BP flake due to its oxidation nature in air. It had N<sub>2</sub> gas and liquid N<sub>2</sub> inlet/outlet to allow the purge of air and the cooling of sample in its chamber.

A BWTEK Voyage confocal Raman system equipped with an external 532 nm laser was used to perform the Raman experiments. The external laser beam was integrated into the Raman system by several optical mirrors, and focused on sample surface by a long working distance 20× objective lens. The focused laser spot size was measured by the knife-edge method, which had a radius of 1.28 μm. The environment cell was mounted on a 3D microstage (5 nm positioning resolution) under the 20× objective lens. The laser beam reached the surface of candidate BP flake through a circular glass window on the top lid of environment cell with negligible energy loss. Collected by the objective lens, Raman signals were acquired by the Raman spectrometer. The integration time of Raman scattering was 1 s, which was a compromising result of minimizing mechanical-drift effect and obtaining strong Raman signals. The ND filter in the Raman system was used to adjust the laser power. Moreover, a half-wave plate was introduced into the optical path to change the laser polarization. After thorough characterization of Raman spectroscopy, AFM was applied to characterize the thickness and morphology of candidate BP flake. The accumulated air-exposure time of candidate BP flake during the mechanical exfoliation, sample preparation, and AFM characterization was less than 30 min, which ensured the oxidation of BP flake was minimal. (Detail settings of the system is depicted in Figure 2a.)

## Supporting Information

Supporting Information is available from the Wiley Online Library or from the author.

## Acknowledgements

The authors gratefully acknowledge the support of this work by National Science Foundation (CBET1235852, CMMI1264399), Department of Energy (DENE0000671, DEEE0007686), and Iowa Energy Center (MG-16-025, OG-17-005).

## Conflict of Interest

The authors declare no conflict of interest.

## Keywords

black phosphorus, interfacial thermal conductance, Raman spectroscopy, thermal expansion

Received: February 23, 2017

Revised: June 11, 2017

Published online:

- [1] A. Castellanos-Gomez, L. Vicarelli, E. Prada, J. O. Island, K. L. Narasimha-Acharya, S. I. Blanter, D. J. Groenendijk, M. Buscema, G. A. Steele, J. V. Alvarez, H. W. Zandbergen, J. J. Palacios, H. S. J. van der Zant, *2D Mater.* **2014**, *1*, 025001.
- [2] F. N. Xia, H. Wang, Y. C. Jia, *Nat. Commun.* **2014**, *5*, 4458.
- [3] L. K. Li, Y. J. Yu, G. J. Ye, Q. Q. Ge, X. D. Ou, H. Wu, D. L. Feng, X. H. Chen, Y. B. Zhang, *Nat. Nanotechnol.* **2014**, *9*, 372.
- [4] H. Liu, A. T. Neal, Z. Zhu, Z. Luo, X. F. Xu, D. Tomanek, P. D. Ye, *ACS Nano* **2014**, *8*, 4033.
- [5] M. Buscema, D. J. Groenendijk, S. I. Blanter, G. A. Steele, H. S. J. van der Zant, A. Castellanos-Gomez, *Nano Lett.* **2014**, *14*, 3347.
- [6] X. Ling, S. X. Huang, E. H. Hasdeo, L. B. Liang, W. M. Parkin, Y. Tatsumi, A. R. T. Nugraha, A. A. Puzos, P. M. Das, B. G. Sumpter, D. B. Geohegan, J. Kong, R. Saito, M. Drndic, V. Meunier, M. S. Dresselhaus, *Nano Lett.* **2016**, *16*, 2260.
- [7] N. N. Mao, J. Y. Tang, L. M. Xie, J. X. Wu, B. W. Han, J. J. Lin, S. B. Deng, W. Ji, H. Xu, K. H. Liu, L. M. Tong, J. Zhang, *J. Am. Chem. Soc.* **2016**, *138*, 300.
- [8] X. M. Wang, A. M. Jones, K. L. Seyler, V. Tran, Y. C. Jia, H. Zhao, H. Wang, L. Yang, X. D. Xu, F. N. Xia, *Nat. Nanotechnol.* **2015**, *10*, 517.
- [9] J. S. Qiao, X. H. Kong, Z. X. Hu, F. Yang, W. Ji, *Nat. Commun.* **2014**, *5*, 4475.
- [10] R. X. Fei, L. Yang, *Nano Lett.* **2014**, *14*, 2884.
- [11] Z. Luo, J. Maassen, Y. X. Deng, Y. C. Du, R. P. Garrelts, M. S. Lundstrom, P. D. Ye, X. F. Xu, *Nat. Commun.* **2015**, *6*, 8527.
- [12] H. J. Jang, J. D. Wood, C. R. Ryder, M. C. Hersam, D. G. Cahill, *Adv. Mater.* **2015**, *27*, 8017.
- [13] S. Lee, F. Yang, J. Suh, S. J. Yang, Y. Lee, G. Li, H. S. Choe, A. Suslu, Y. B. Chen, C. Ko, J. Park, K. Liu, J. B. Li, K. Hippalgaonkar, J. J. Urban, S. Tongay, J. Q. Wu, *Nat. Commun.* **2015**, *6*, 8573.
- [14] B. Sun, X. Gu, Q. Zeng, X. Huang, Y. Yan, Z. Liu, R. Yang, Y. K. Koh, *Adv. Mater.* **2017**, *29*, 1603297.
- [15] B. Smith, B. Vermeersch, J. Carrete, E. Ou, J. Kim, N. Mingo, D. Akinwande, L. Shi, *Adv. Mater.* **2017**, *29*, 1603756.
- [16] H. Chen, P. Huang, D. Guo, G. X. Xie, *J. Phys. Chem. C* **2016**, *120*, 29491.
- [17] H. Y. Sun, G. Liu, Q. F. Li, X. G. Wan, *Phys. Lett. A* **2016**, *380*, 2098.
- [18] J. W. Jiang, H. S. Park, *J. Phys. D: Appl. Phys.* **2014**, *47*, 385304.
- [19] Q. Wei, X. H. Peng, *Appl. Phys. Lett.* **2016**, *104*, 251915.
- [20] J. C. Zhang, Y. Hong, M. Q. Liu, Y. N. Yue, Q. G. Xiong, G. Lorenzini, *Int. J. Heat Mass Transfer* **2017**, *104*, 871.
- [21] Y. N. Yue, J. C. Zhang, X. W. Wang, *Small* **2011**, *7*, 3324.
- [22] X. D. Tang, S. Xu, J. C. Zhang, X. W. Wang, *ACS Appl. Mater. Interfaces* **2014**, *6*, 2809.
- [23] P. Yuan, C. Li, S. Xu, J. Liu, X. Wang, *Acta Mater.* **2017**, *122*, 152.
- [24] J. D. Wood, S. A. Wells, D. Jariwala, K. S. Chen, E. Cho, V. K. Sangwan, X. L. Liu, L. J. Lauhon, T. J. Marks, M. C. Hersam, *Nano Lett.* **2014**, *14*, 6964.
- [25] R. A. Doganov, E. C. T. O'Farrell, S. P. Koenig, Y. T. Yeo, A. Ziletti, A. Carvalho, D. K. Campbell, D. F. Coker, K. Watanabe, T. Taniguchi, A. H. C. Neto, B. Ozyilmaz, *Nat. Commun.* **2015**, *6*, 6647.
- [26] A. Favron, E. Gaufres, F. Fossard, A. L. Phaneuf-L'Heureux, N. Y. W. Tang, P. L. Levesque, A. Loiseau, R. Leonelli, S. Francoeur, R. Martel, *Nat. Mater.* **2015**, *14*, 826.
- [27] D. J. Late, *ACS Appl. Mater. Interfaces* **2015**, *7*, 5857.
- [28] T. L. Bergman, F. P. Incropera, D. P. DeWitt, A. S. Lavine, *Fundamentals of Heat and Mass Transfer*, John Wiley & Sons, Hoboken **2011**, p. 985.
- [29] J. G. Weaver, H. P. R. Frederikse, *Optical Properties of Selected Elements CRC Handbook of Chemistry and Physics*, 87th ed., CRC Press, Boca Raton **2007**, p. 12–116.
- [30] H. P. Li, R. Q. Zhang, *EPL* **2012**, *99*, 36001.
- [31] A. Taube, J. Judek, A. Lapiriska, M. Zdrojek, *ACS Appl. Mater. Interfaces* **2015**, *7*, 5061.
- [32] D. Yoon, Y. W. Son, H. Cheong, *Nano Lett.* **2011**, *11*, 3227.
- [33] L. Q. Su, Y. Zhang, Y. F. Yu, L. Y. Cao, *Nanoscale* **2014**, *6*, 4920.
- [34] L. Q. Su, Y. F. Yu, L. Y. Cao, Y. Zhang, *Nano Res.* **2015**, *8*, 2686.
- [35] C. A. Swenson, *J. Phys. Chem. Ref. Data* **1983**, *12*, 179.
- [36] B. Huang, Y. K. Koh, *Carbon* **2016**, *105*, 286.
- [37] P. E. Hopkins, *ISRN Mech. Eng.* **2013**, *2013*, 1.
- [38] R. J. Stevens, L. V. Zhigilei, P. M. Norris, *Int. J. Heat Mass Transfer* **2007**, *50*, 3977.
- [39] A. H. Al-Bayati, K. G. Orrman-Rossiter, J. A. van den Berg, D. G. Armour, *Surf. Sci.* **1991**, *241*, 91.
- [40] M. Morita, T. Ohmi, E. Hasegawa, M. Kawakami, M. Ohwada, *J. Appl. Phys.* **1990**, *68*, 1272.
- [41] A. Castellanos-Gomez, M. Buscema, R. Molenaar, V. Singh, L. Janssen, H. S. J. van der Zant, G. A. Steele, *2D Mater* **2014**, *1*, 011002.